Imaging spin-resolved cyclotron trajectories in the InSb two-dimensional electron gas

A. Mreńca-Kolasińska, K. Kolasiński, and B. Szafran
AGH University of Science and Technology, Faculty of Physics and Applied Computer Science, al. Mickiewicza 30, 30-059 Kraków, Poland

(Received 7 June 2018; revised manuscript received 30 August 2018; published 28 September 2018)

We consider spin-resolved cyclotron trajectories in a magnetic focusing device with quantum point source and drain contacts defined within the InSb two-dimensional electron gas and their mapping by the scanning gate microscopy. Besides the perpendicular component of the external magnetic field which bends the electron trajectories, we consider an in-plane component which introduces the spin dependence of the cyclotron radius. We demonstrate that the focusing conductance peaks become spin split by the in-plane magnetic field component on the order of a few tesla and that the spin-resolved trajectories can be traced separately with the conductance mapping.

DOI: 10.1103/PhysRevB.98.115309

I. INTRODUCTION

The separation and control of the electron spins in the two-dimensional electron gas (2DEG) has been a subject of intense investigation in the field of spintronics [1]. In the external magnetic field the focusing of the cyclotron trajectories can be detected in a setup with quantum point contact (QPC) source and drain terminals [2–12]. In this work we consider the spin-dependent trajectories that could be resolved in the magnetic focusing experiment [2–12] by the scanning gate microscopy [13]. The focusing of electron trajectories for carriers injected across the QPC with spins separated by spin-orbit interaction (SOI) was considered theoretically [14–20] and studied experimentally [7–11,21]. The spin separation by the strong spin-orbit interaction is achieved by splitting the magnetic focusing peaks with the orthogonal spin polarization for electrons that pass across the quantum point contacts. The spin-orbit coupling alone in the absence of the external magnetic field has also been proposed for the spin separation in InGaAs QPCs [22] and in U- [23] or Y-shaped [24] junctions of topological insulators. However, for strong spin-orbit coupling the electron spin precesses in the effective momentum-dependent spin-orbit magnetic field [25,26] that is oriented within the plane of confinement of the carrier gas. In this work we indicate a possibility of imaging the spin-resolved electron trajectories for which the electron spin is fixed and the spin precession in the spin-orbit field is frozen by strong Zeeman effect due to an in-plane magnetic field. For that purpose instead of the spin-orbit coupling [7–11,14,17,19] we use an in-plane magnetic field [27–29] component that introduces the spin dependence of the cyclotron trajectories by the Zeeman splitting. We demonstrate that for the indium antimonide—a large Landé factor material—the spin-dependent electron trajectories can be clearly resolved by the scanning gate microscopy technique.

In the focusing experiments with the 2DEG the electrons are injected and gathered by QPCs [30–32]. The constrictions formed in 2DEG by electrostatic gates depleting the electron gas lead to the formation of transverse quantized modes. By applying sufficiently high potential on the gates only one or a few modes can adiabatically pass through the QPC. The quantized plateaus of conductance of such constrictions have been recently reported in InSb [33].

The scanning gate microscopy (SGM) is an experimental technique in which a charged tip of an atomic force microscope is raster-scanned over a sample while measuring the conductance [13]. The tip acts as a movable gate that can locally deplete the 2DEG, with a possible effect on the conductance. The SGM technique has been used in 2DEG confined in III-V nanostructures for example to image the branching of the current trajectories in systems with QPC and the interference of electrons backscattered between the tip and the QPC [34–37], the scarred wave functions in quantum billiards [38,39], and electron cyclotron trajectories [6,40]. It has been used for imaging the cyclotron motion also in two-dimensional materials like graphene [41,42].

II. MODEL AND THEORY

We consider quantum transport at the Fermi level in 2DEG confined within an InSb quantum well. The model system depicted in Fig. 1 contains two QPCs on the left-hand side, and is open on the right-hand side. The electrostatically defined two quantum point contacts are separated by a distance L. The terminals are numbered as indicated in Fig. 1. The electrons entering from lead 1 are injected trough the first (lower) QPC into the system in a narrow beam that is steered by the transverse magnetic field. Whenever the cyclotron diameter (or its integer multiple) fits the separation L, electrons can enter the second QPC which serves as a collector. Electrons that do not get to the collector exit the system through lead 3, which is used as open boundary conditions. Hard wall boundary conditions are introduced on the perpendicular edges of the computational box. The size of the computational box (width $W = 2400$ nm and length 1800 nm) is large enough to make the effects of the scattering by the hard wall boundaries negligible for the drain (lead 2) currents.

For the transport modeling we assume that the vertical confinement in the InSb quantum well is strong enough to justify the two-dimensional approximation for the electron

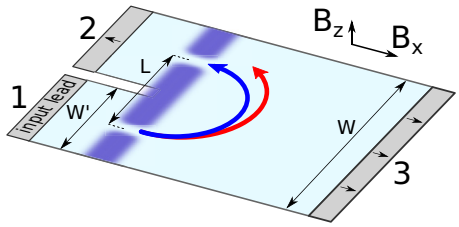

FIG. 1. The scheme of the focusing system. The dark blue shaded area is the gate-induced potential defining the two QPCs, separated by the distance L. The spin up (spin down) is parallel (antiparallel) to the total magnetic field. Due to the in-plane magnetic field (and hence Zeeman splitting) the spin-up and spin-down electrons have different momenta and get spatially separated due to the difference in the cyclotron radii. The red and blue arrows correspond to spin-up and spin-down electron trajectories, respectively. The gray rectangles indicate the open boundary conditions. The terminals are numbered by integers from 1 to 3. Terminal 1 (2) is the source (drain) of the currents. Terminal 3 plays the role of an open boundary.

motion. The 2D effective mass Hamiltonian reads

$$H = \left[\frac{\hbar^2}{2m_{\text{eff}}}\mathbf{k}^2 + eV(\mathbf{r})\right]\mathbf{1} + \tfrac{1}{2}\mu_B \mathbf{B}^T \mathbf{g}^* \boldsymbol{\sigma} + H_{\text{SO}}, \quad (1)$$

where $\mathbf{k} = -i\nabla - e\mathbf{A}$, with $\mathbf{A}$ being the vector potential, $\mathbf{B} = (B_x, B_y, B_z)$, $\boldsymbol{\sigma}$ is the vector of Pauli matrices, μ_B is the Bohr magneton, $\mathbf{g}^*$ is the diagonal Landé tensor, and m_{eff} is the electron effective mass in InSb.

The external potential as seen by the Fermi level electrons is a superposition of the QPC and the potential induced by the charged SGM tip

$$V(\mathbf{r}) = V_{\text{QPC}}(\mathbf{r}) + V_{\text{tip}}(\mathbf{r}), \quad (2)$$

where we model the QPC using the analytical formulas developed in [43] with electrostatic potential of a finite rectangular gate given by

$$\begin{aligned} V_r(\mathbf{r}; l, r, b, t) = V_g[&g(x-l, y-b) + g(x-l, t-y) \\ &+ g(r-x, y-b) + g(r-x, t-y)], \end{aligned} \quad (3)$$

where $g(u, v) = \frac{1}{2\pi}\arctan\left(\frac{uv}{u^2+v^2+d^2}\right)$ with $d = 50$ nm, and V_g is the potential applied to the gates. The QPC potential is a superposition of potentials of three such gates

$$\begin{aligned} V_{\text{QPC}} = &V_r(\mathbf{r}; l, r, b_1, t_1) + V_r(\mathbf{r}; l, r, b_2, t_2) \\ &+ V_r(\mathbf{r}; l, r, b_3, t_3). \end{aligned} \quad (4)$$

The gates and their labeling used in Eq. (4) are schematically shown in Fig. 2. The splitting of the gates is $d_{\text{QPC}} = 105$ nm defining the QPC width. The QPCs are separated by $L = 1200$ nm.

For modeling the tip potential we use a Gaussian profile

$$V_{\text{tip}}(\mathbf{r}) = V_t \exp\left[-\frac{(x - x_{\text{tip}})^2 + (y - y_{\text{tip}})^2}{d_{\text{tip}}^2}\right], \quad (5)$$

with V_t being the maximum tip potential, d_{tip} its width, and x_{tip}, y_{tip} the coordinates of the tip.

The spin-orbit interactions in InSb are strong, so we include them in the calculations. The two last terms in (1)

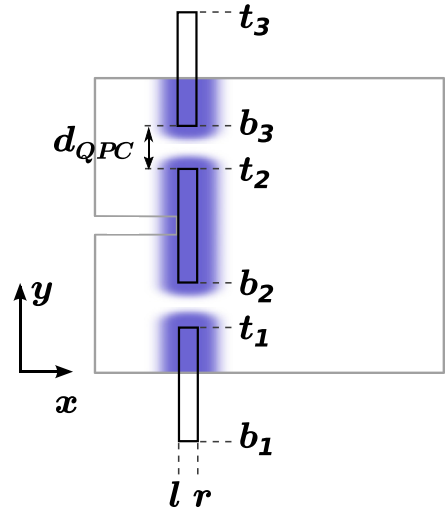

FIG. 2. The scheme of the gates inducing the potential of the two QPCs. The figure is not to scale. The values of the geometrical parameters are: $l = 300$ nm, $r = 500$ nm, $b_1 = -600$ nm, $t_1 = 547$ nm, $t_2 = 652$ nm, $b_2 = 1747$ nm, $b_3 = 1852$ nm, and $t_3 = 3000$ nm.

account for the SOI with $H_{\text{SO}} = H_R + H_D$, where

$$H_R = \alpha(-k_x\sigma_y + k_y\sigma_x) \quad (6)$$

describes the Rashba interaction, and

$$H_D = \beta(k_x\sigma_x - k_y\sigma_y) \quad (7)$$

the Dresselhaus interaction. For the Hamiltonian (1) we use the parameters for InSb quantum well, $\alpha = -0.051$ eV Å, $\beta = 0.032$ eV Å, $g^*_{zz} = -51$ [44], $g^*_{xx} = \frac{1}{2}g^*_{zz}$ [33], $m_{\text{eff}} = 0.018m_0$ [33].

We perform the transport calculations in the finite difference formalism. For evaluation of the transmission probability, we use the wave function matching (WFM) technique [45]. The transmission probability from the input lead to mode m with spin σ in the output lead is

$$T^m_\sigma = \sum_{n,\sigma'} \left|t^{mn}_{\sigma\sigma'}\right|^2, \quad (8)$$

where $t^{mn}_{\sigma\sigma'}$ is the probability amplitude for the transmission from the mode n with spin σ' in the input lead to mode m with spin σ in the output lead. We evaluate the conductance as $G = G_0 \sum_{m,\sigma} T^m_\sigma$, with $G_0 = e^2/h$.

The considered system presented in Fig. 1 has the width $W = 2400$ nm, and the narrow leads numbered 1 and 2 have equal width $W' = 1146$ nm. The spacing between the centers of the QPCs is $L = 1200$ nm. We take the gate potential $V_g = 62$ meV, for which at $E_F = 26$ meV in the absence of the external magnetic field the QPC conductance is close to $2\frac{e^2}{h}$. For the SGM we use the tip parameters $V_t = 260$ meV, and $d_{\text{tip}} = 60$ nm.

III. RESULTS

A. No in-plane magnetic field

Let us first consider the transport in the system with the out-of-plane magnetic field only (i.e., $B_x = 0$, $B_y = 0$,

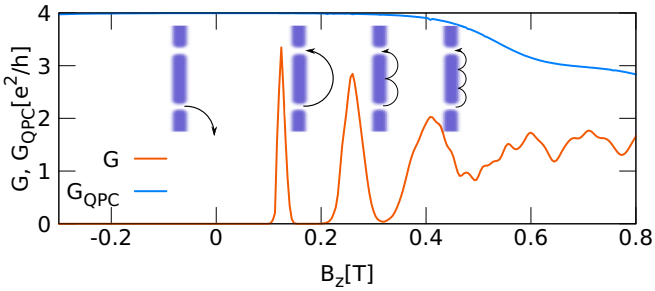

FIG. 3. The conductance from the left bottom to the left top lead G as a function of magnetic field and the lower QPC conductance $G_{\rm QPC}$. The inset shows semiclassical trajectories of the electrons for $B_z < 0$, and at the three focusing peaks $B_z^{(i)}$ with $i = 1, 2, 3$.

$B_z \neq 0$). In Fig. 3 we present the conductance $G = G_{21}$ from lead 1 to lead 2 as a function of the applied transverse magnetic field, and the summed conductance from lead 1 to leads 2 and 3, which is essentially the conductance of the lower QPC $G_{\rm QPC} = G_{21} + G_{31}$. For $B_z < 0$ no focusing peaks occur because the electrons are deflected in the opposite direction than the collector, propagate along the bottom edge of the system, and finally exit through the right lead. For $B_z > 0$ conductance peaks almost equidistant in magnetic field appear. The first three maxima occur at $B_z^{(1)} = 0.124$ T, $B_z^{(2)} = 0.26$ T, $B_z^{(3)} = 0.408$ T. Neglecting the SOI terms and the Zeeman term in (1), one obtains $|k_F| = \sqrt{2m_{\rm eff}E_F} = 0.2148\frac{1}{\rm nm}$. For the cyclotron diameter equal to

$$D_c = \frac{2\hbar|k_F|}{|e|B_z}, \tag{9}$$

one obtains for the first three peaks $D_c^{(1)} = 1176$ nm, $D_c^{(2)} = 561$ nm, $D_c^{(3)} = 358$ nm, respectively. This is close to the distance between the centers of the QPCs, $L = 1200$ nm, its half, $L/2 = 600$ nm, and one third, $L/3 = 400$ nm, respectively. Despite the high spin-orbit interaction in the InSb quantum well, no spin splitting occurs. Let us denote the Fermi wave number of the subband of spin σ by k_F^σ. For the adapted values of the SO parameters, the difference in momenta for both spins is small [see Fig. 4(a)]. For example for $k_{F,y}^\uparrow, k_{F,y}^\downarrow = 0$ and $E_F = 26$ meV, the x components extracted from the dispersion relation in Fig. 4(a) are $|k_{F,x}^\uparrow| = 0.11445$ nm^{-1}, and $|k_{F,x}^\downarrow| = 0.11142$ nm^{-1}, that for $D_c = 1200$ nm yield transverse magnetic field $B_z^{(1)} = 0.125$ T and $B_z^{(1)} = 0.122$ T,

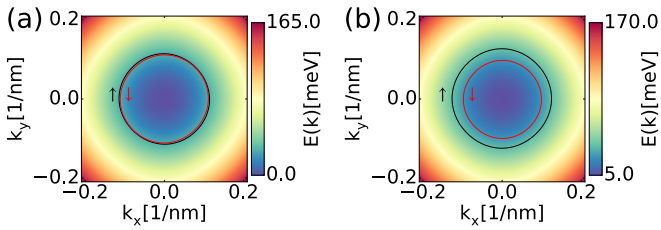

FIG. 4. Dispersion relation of the 2DEG with (a) $B_x = 0$ and (b) $B_x = 8$ T. The color map shows the dispersion relation of the spin-down band, and the contours show the isoenergetic lines for $E_f = 26$ meV for spin-up (black line) and spin-down (red line) electrons.

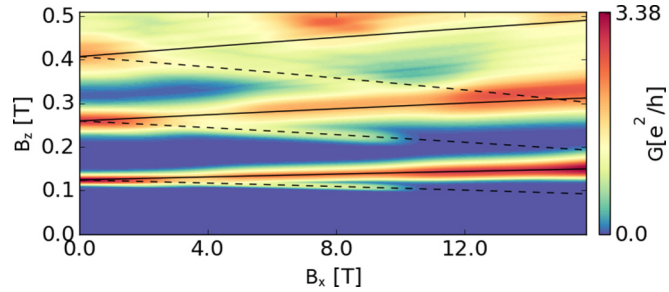

FIG. 5. Transmission as a function of B_x and B_z. The solid (dashed) lines are the analytically calculated positions of transmission peaks maxima for spin-up (spin-down) electrons.

respectively. That is clearly too small a difference to obtain a visible double peak.

B. Enhancement of the Zeeman splitting with in-plane magnetic field

In the next step we apply an additional in-plane magnetic field. This leads to an increase of the Zeeman energy splitting for both spins leading to the increase of the momenta difference between both spin subbands. Figure 4 shows the momenta for both spins for $B_x = 0$ and 8 T. Without in-plane magnetic field, the spin subbands are nearly degenerate. With B_x on the order of a few tesla the difference in the momenta becomes significant. This induces a change of the cyclotron radii of the electrons with opposite spins.

The spins are oriented along the total magnetic field $\mathbf{B} + \mathbf{B}_{\rm SO}$, where $\mathbf{B}_{\rm SO}$ is the effective SO field. For B_x on the order of a few tesla the out-of-plane magnetic field component and the SO effective field are small compared to the in-plane component. The spin is oriented nearly along the x or $-x$ direction. We refer to these states as spin up and spin down.

Figure 5 shows the conductance G from lead 1 to lead 2 as a function of the in-plane (here B_x) and the transverse magnetic fields. For a sufficiently high in-plane magnetic field the peaks split, with the splitting growing with increasing B_x. The lines plotted along the nth pair of split peaks are calculated from the condition $B_{z,\sigma}^{(n)}(B_x) = \frac{2\hbar|k_F^\sigma|}{|e|D_c^{(n)}}$, with $|k_F^\sigma|$ obtained from

$$E_F = \frac{(\hbar k_F^\sigma)^2}{2m_{\rm eff}} \pm \frac{1}{2} g_{xx}^* \mu_B B_x, \tag{10}$$

where $\sigma = \uparrow, \downarrow$, the $\pm$ sign corresponds to spin down and up, respectively, and $D_c^{(n)}$ are extracted from Fig. 3, using Eq. (9). Although the analytical lines are obtained neglecting the SOI and the Zeeman energy contribution from the transverse magnetic field, there is a good agreement between the obtained transport results and this simplified model.

The cross section of the summed conductance and the spin-resolved conductance for $B_x = 8$ T is shown in Fig. 6. In the pairs of focusing peaks, the spin-down (spin-up) conductance dominates for the peak at lower (higher) magnetic field [see Fig. 6(b)]. Interestingly, in each pair of the peaks in Fig. 5, the lower one has a smaller transmission than the upper one, and at $B_x \approx 10$ T vanishes, while the transmission of the upper one slowly increases. The reason for this behavior is the strong Zeeman splitting due to the in-plane magnetic field and

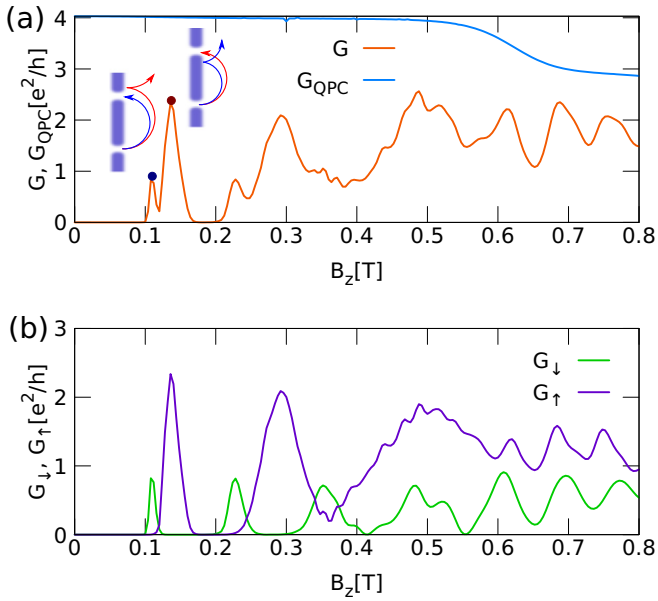

FIG. 6. (a) The cross section of the conductance and the lower QPC conductance for $B_x = 8$ T. (b) The spin-resolved conductance. The first peak is split into two smaller peaks with $B^{(1)}_{z,\downarrow} = 0.11$ T for spin-down electrons and $B^{(1)}_{z,\uparrow} = 0.137$ T for spin-up electrons. The inset in (a) shows semiclassical trajectories of the spin-up (red semicircles) and spin-down (blue semicircles) electron at the first focusing peak.

the spin-dependent conductance of the QPCs [5,46]. Figure 7 shows the dispersion relation of an infinite channel with the lateral potential taken at the QPC constriction with applied $B_x = 0$, 8, and 12 T. For $B_x = 8$ T at the Fermi level for spin up three transverse subbands are available, while for spin down only one. For higher $B_x = 12$ T the spin-down subband is raised above the Fermi level, and only spin-up electrons can pass through the QPC. On the other hand, for growing B_x, the number of spin-up subbands increases. Thus in the focusing spectrum, the upper peak—the spin-up peak—becomes more pronounced, while the lower one—the spin-down peak—has a lower value of transmission and finally disappears.

Concluding this section, we find that the in-plane magnetic field allows for a controllable separation of the electrons with opposite spins. It is worth noting that in the systems that have

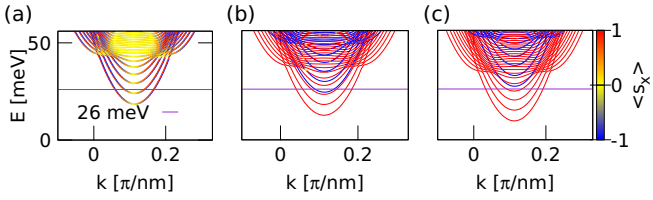

FIG. 7. Dispersion relation of an infinite channel with the lateral potential taken at the QPC constriction with $V_r = 62$ meV, and (a) $B_x = 0$ T, (b) $B_x = 8$ T, and (c) 12 T. The color map shows the mean x spin component of the subband. The spin-down subband shifts up in energy upon increasing B_x and finally is raised above the Fermi energy. The opposite occurs for the spin-up electrons—for increasing B_x more and more subbands are available at the Fermi level.

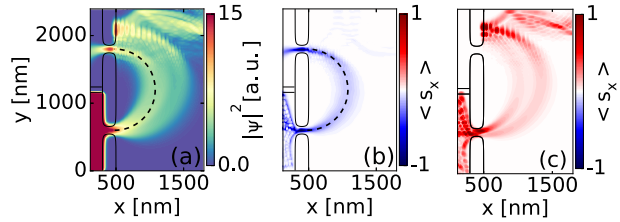

FIG. 8. The density and average spins maps for the low-field peak in Fig. 6. In (b) the average spin x projection for a spin-down mode is shown, and in (c) for a spin-up mode. The spin in the y and z directions is negligibly small (not shown), and the average spin in the x direction is preserved (cf. Fig. 13 for the spin precession effects in the case where SOI dominates over the Zeeman interaction).

strong SOI, without the in-plane magnetic field, only the odd focusing peaks get split [8,14,26], and in the case of the in-plane magnetic field all of the peaks are split. This is caused by the spin precession due to SOI in those systems. In our case the spin is determined by the effective magnetic field, which is almost parallel to x direction. Thus the spin in x direction dominates and the fluctuation due to SOI is negligible. It is shown in a representative case of the density and average spins for the low-field focusing peak at $B^{(1)}_{z,\downarrow} = 0.11$ T in Fig. 8. The electron spins are nearly unchanged along the entire path. The $\langle s_y \rangle$ and $\langle s_z \rangle$ are negligibly small compared to the $\langle s_x \rangle$.

C. Scanning gate microscopy of the trajectories

We simulated the SGM conductance maps for the magnetic fields that correspond to the peaks of magnetic focusing in the absence of the tip. We used $B_x = 8$ T. In the cross section for $B_x = 8$ T in Fig. 6(a) the dots show where the SGM scans were taken. Figure 9 presents the maps of $\Delta G = G(\mathbf{r}_{\text{tip}}) - G(B^{(1)}_{z,\sigma})$, and the spin-resolved conductances $\Delta G_{\sigma'} = G_{\sigma'}(\mathbf{r}_{\text{tip}}) - G_{\sigma'}(B^{(1)}_{z,\sigma})$ with $\sigma, \sigma' = \uparrow, \downarrow$. The conductance maps exhibit semicircular pattern with a pronounced minimum along the semiclassical orbit of a carrier incident in the x direction (indicated in Fig. 9 with dashed semicircles). For the spin-up focusing peak at $B^{(1)}_{z,\downarrow} = 0.11$ T, the scan [Fig. 9(a)] is slightly different than for the spin-down peak at $B^{(1)}_{z,\uparrow} = 0.137$ T [Fig. 9(b)]. In the first one there is a slight increase of conductance to the right of the dashed semicircle [see the red blob in Fig. 9(a)]. Figures 9(c) and 9(d) show the spin-up conductance, and Figs. 9(e) and 9(f) the spin-down conductance as a function of the tip position. One can see that in the spin-down peak (for $B^{(1)}_{z,\downarrow} = 0.11$ T) the $\Delta G_{\downarrow}$ is everywhere negative or zero [Fig. 9(e)], and $\Delta G_{\uparrow}$ is positive or zero almost everywhere (except within the QPC) [Fig. 9(c)]. Examples of electron densities with the tip placed in two different points are shown in Fig. 10. In Fig. 10(a), the tip, when placed along the electron trajectory, leads to the deflection of the beam and blocks the spin-down beam, preventing it from entering the collector. On the other hand, in Fig. 10(b), the tip can deflect the beam of spin-up electrons into the collector.

The situation is inverted in the peak at $B_z = 0.137$ T. In the $\Delta G_{\uparrow}$ map [Fig. 9(d)], the values are smaller or equal to zero, and in the $\Delta G_{\downarrow}$ map [Fig. 9(f)], bigger or equal to zero. In this

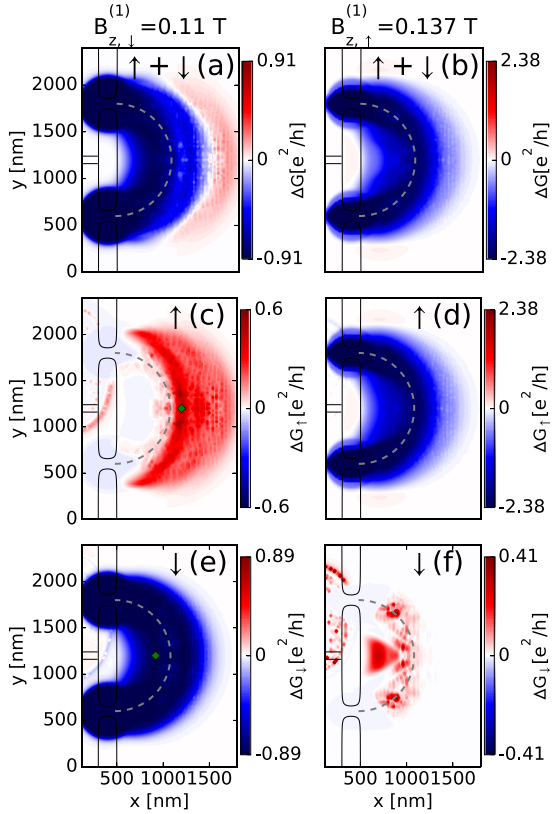

FIG. 9. The conductance maps for the spin-down (left column) and spin-up (right column) focusing peak in Fig. 6 at $B^{(1)}_{z,\downarrow} = 0.11$ T and $B^{(1)}_{z,\uparrow} = 0.137$ T, respectively. (a) and (b) Conductance summed over spins, (c) and (d) the spin-up conductance, and (e) and (f) the spin-down conductance. The dashed semicircles show the semiclassical trajectory of an electron incident from the QPC with $k_x \neq 0$ only. The tiny arrows in the upper right corner show which contribution of ΔG is shown in the plot.

case, the spin-up beam is blocked by the tip, thus $\Delta G_\uparrow$ drops along the semicircle marked in Fig. 9(d). On the other hand, the spin-down electrons have a smaller cyclotron diameter (than the QPC spacing L), but they can be scattered by the

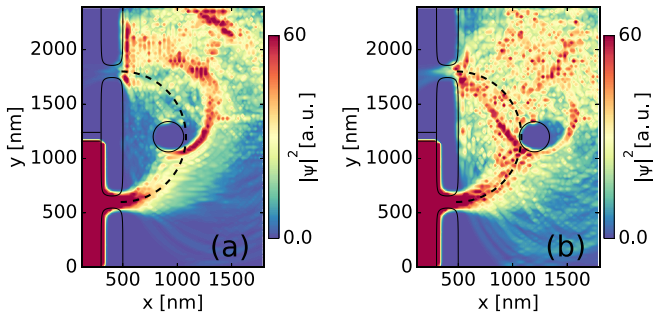

FIG. 10. The density maps for the tip placed in the points marked with diamonds in Figs. 9(c) and 9(e). (a) The tip blocking the beam with the tip at the point marked with green diamond in Fig. 9(c). (b) The tip enabling the spin-up beam to enter the collector with the tip at the point marked with green diamond in Fig. 9(e).

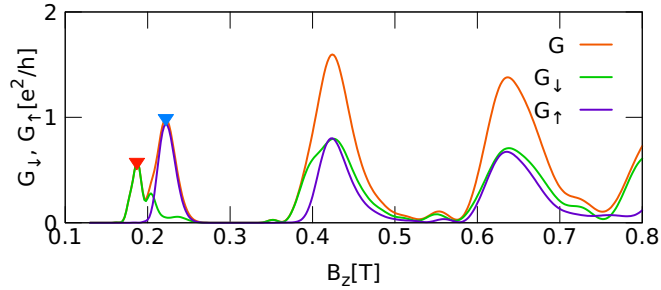

FIG. 11. (a) The summed and spin-resolved conductance for a hole system in the GaAs/AlGaAs system. The first peak is split into two smaller peaks with $B^{(1)}_{z,\downarrow} = 0.187$ T for spin-down holes and $B^{(1)}_{z,\uparrow} = 0.222$ T for spin-up holes. The peak splitting is 35 mT.

tip to the collector, which leads to an increase of ΔG at some points to the left of (or along) the dashed semicircle.

D. Magnetic focusing for heavy holes in GaAs/AlGaAs heterostructure

We consider an experiment conducted for two-dimensional hole gas (2DHG) in GaAs/AlGaAs, in Ref. [10], where the splitting of the first focusing peak was visible without an in-plane magnetic field, and was solely due to the spin-orbit interaction. For this problem we assume the distance between the two QPCs $L = 800$ nm, the computational box of width $W = 1608$ nm, and length 3000 nm, the QPC defined in the same manner as in Eq. (4) with the geometrical parameters: $l = 500$ nm, $r = 1100$ nm, $b_1 = -600$ nm, $t_1 = 336$ nm, $t_2 = 468$ nm, $b_2 = 1140$ nm, $b_3 = 1272$ nm, $t_3 = 2208$ nm, and $d = 20$ nm. We employ the effective mass of heavy holes $m_{\text{eff}} = 0.17 m_e$ [47], Landé factor $g^*_{zz} = -0.6$ [48], the Dresselhaus SO parameter $\beta = 0.0477$ eV Å [10], and zero Rashba SO.

We tune the lower QPC to $G_{\text{QPC}} = 2e^2/h$, with $V_g = 18$ meV, and $E_F = 3.2$ meV. Figure 11 shows the focusing conductance of the system. The focusing peaks are resolved, with the first peak split by 35 mT, remarkably close to the result in Ref. [10], with the measured splitting of 36 mT. The splitting is due to the Dresselhaus SOI, which leads to the spin polarization in the direction dependent on the hole momentum, and the difference in the Fermi wave numbers k_F

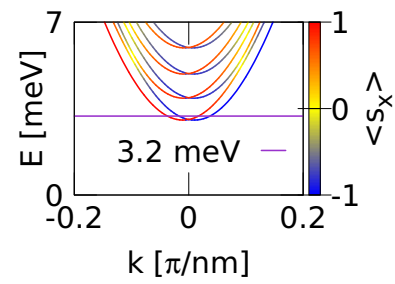

FIG. 12. Dispersion relation of an infinite channel with the lateral potential taken at the QPC constriction with $V_r = 18$ meV and $B_x = 0$ T. The color map shows the mean x spin component of the subbands.

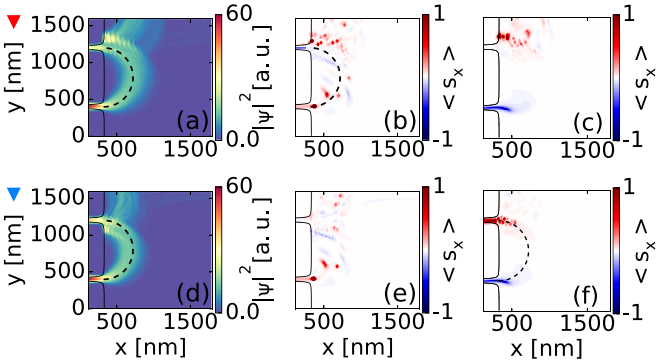

FIG. 13. The density and average spin x component maps for the focusing marked peaks in Fig. 11, for the low-field peak marked with a red triangle (upper row) and high-field peak marked with a blue triangle (lower row). (a) and (b) The densities, (b) and (e) the average spin for the injected spin-up mode, and (c) and (f) for the injected spin-down mode. The flip of the spin direction in the detector QPC is visible.

of the holes with opposite spins. The band structure in the injector QPC is shown in Fig. 12. The hole spin in the injector QPC is in the x direction.

The difference in focusing magnetic field due to SOI can be evaluated by

$$B^{(1)}_{z,\sigma} = \frac{2\hbar k^{\sigma}_F}{eD^{(1)}_c} = \frac{\sqrt{2m_{\rm eff}E_F} \mp m_{\rm eff}\beta\hbar}{eD^{(1)}_c}. \qquad (11)$$

The density and the spin evolution in the peaks highlighted in Fig. 11 by tiny triangles is shown in Fig. 13. In the densities [Figs. 13(a) and 13(d)] the contributions of both spins with slightly different cyclotron radii are visible. In the averaged spin x component maps for the mode injected with spin up [Figs. 13(b) and 13(e)] the precession is visible, but a little blurred due to the scattering from the gates' potential. For the mode injected with spin down [Figs. 13(c) and 13(f)] the flip of the spin direction in the detector is clearly visible.

IV. SUMMARY AND CONCLUSIONS

We have studied the spatial spin splitting of the electron trajectories in the transverse focusing system. We demonstrated that the in-plane magnetic field of a few tesla in InSb induces the Zeeman splitting which is large enough to separate the conductance focusing peaks for the spin-down and spin-up Fermi levels. The orientation of the spin is translated to the position of the conductance peak on the magnetic field scale. The focused trajectories for both spin orientations can be resolved by the scanning gate microscopy conductance maps. Moreover, the SGM maps for opposite spin peaks contain qualitative differences due to the spin dependence of the cyclotron radii. The present finding paves the way for studies of the spin-dependent trajectories in the systems with the two-dimensional electron gas with high Landé factor materials.

ACKNOWLEDGMENTS

This work was supported by the National Science Centre (NCN) Grant No. DEC-2015/17/N/ST3/02266, and by AGH UST budget with the subsidy of the Ministry of Science and Higher Education, Poland with Grant No. 15.11.220.718/6 for young researchers and Statutory Task No. 11.11.220.01/2. The calculations were performed on PL-Grid and ACK CYFRONET AGH Infrastructure.

[1] S. A. Wolf, D. D. Awschalom, R. A. Buhrman, J. M. Daughton, S. von Molnár, M. L. Roukes, A. Y. Chtchelkanova, and D. M. Treger, Science **294**, 1488 (2001).
[2] Yu. V. Sharvin, Zh. Eksp. Teor. Fiz. **48**, 984 (1965) [Sov. Phys. JETP **21**, 655 (1965)].
[3] V. S. Tsoi, Pis'ma Zh. Eksp. Teor. Fiz. **19**, 114 (1974) [JETP Lett. **19**, 70 (1974)].
[4] H. van Houten, C. W. J. Beenakker, J. G. Williamson, M. E. I. Broekaart, P. H. M. van Loosdrecht, B. J. van Wees, J. E. Mooij, C. T. Foxon, and J. J. Harris, Phys. Rev. B **39**, 8556 (1989).
[5] R. Hanson, B. Witkamp, L. M. K. Vandersypen, L. H. W. van Beveren, J. M. Elzerman, and L. P. Kouwenhoven, Phys. Rev. Lett. **91**, 196802 (2003).
[6] K. E. Aidala, R. E. Parrott, T. Kramer, E. J. Heller, R. M. Westervelt, M. P. Hanson, and A. C. Gossard, Nat. Phys. **3**, 464 (2007).
[7] A. Dedigama, D. Deen, S. Murphy, N. Goel, J. Keay, M. Santos, K. Suzuki, S. Miyashita, and Y. Hirayama, Physica E **34**, 647 (2006).
[8] S.-T. Lo, C.-H. Chen, J.-C. Fan, L. W. Smith, G. L. Creeth, C.-W. Chang, M. Pepper, J. P. Griffiths, I. Farrer, H. E. Beere, G. A. C. Jones, D. A. Ritchie, and T.-M. Chen, Nat. Commun. **8**, 15997 (2017).
[9] C. Yan, S. Kumar, M. Pepper, P. See, I. Farrer, D. Ritchie, J. Griffiths, and G. Jones, Nanoscale Res. Lett. **12**, 553 (2017).
[10] L. P. Rokhinson, V. Larkina, Y. B. Lyanda-Geller, L. N. Pfeiffer, and K. W. West, Phys. Rev. Lett. **93**, 146601 (2004).
[11] S. Chesi, G. F. Giuliani, L. P. Rokhinson, L. N. Pfeiffer, and K. W. West, Phys. Rev. Lett. **106**, 236601 (2011).
[12] L. P. Rokhinson, L. N. Pfeiffer, and K. W. West, Phys. Rev. Lett. **96**, 156602 (2006).
[13] H. Sellier, B. Hackens, M. G. Pala, F. Martins, S. Baltazar, X. Wallart, L. Desplanque, V. Bayot, and S. Huant, Semicond. Sci. Technol. **26**, 064008 (2011).
[14] G. Usaj and C. A. Balseiro, Phys. Rev. B **70**, 041301 (2004).
[15] U. Zülicke, J. Bolte, and R. Winkler, New J. Phys. **9**, 355 (2007).
[16] A. Reynoso, G. Usaj, and C. A. Balseiro, Phys. Rev. B **75**, 085321 (2007).
[17] J. Schliemann, Phys. Rev. B **77**, 125303 (2008).
[18] A. A. Reynoso, G. Usaj, and C. A. Balseiro, Phys. Rev. B **78**, 115312 (2008).
[19] A. Kormányos, Phys. Rev. B **82**, 155316 (2010).
[20] S. Bladwell and O. P. Sushkov, Phys. Rev. B **92**, 235416 (2015).
[21] C. Yan, S. Kumar, M. Pepper, K. Thomas, P. See, I. Farrer, D. Ritchie, J. Griffiths, and G. Jones, J. Phys. Conf. Ser. **964**, 012002 (2018).
[22] M. Kohda, S. Nakamura, Y. Nishihara, K. Kobayashi, T. Ono, J.-i. Ohe, Y. Tokura, T. Mineno, and J. Nitta, Nat. Commun. **3**, 1082 (2012).
[23] M. Zeng and G. Liang, J. Appl. Phys. **112**, 073707 (2012).

[24] G. Gupta, H. Lin, A. Bansil, M. B. Abdul Jalil, C.-Y. Huang, W.-F. Tsai, and G. Liang, Appl. Phys. Lett. **104**, 032410 (2014).
[25] L. Meier, G. Salis, I. Shorubalko, E. Gini, S. Schön, and K. Ensslin, Nat. Phys. **3**, 650 (2007).
[26] A. Reynoso, G. Usaj, and C. Balseiro, in *Quantum Magnetism*, edited by B. Barbara, Y. Imry, G. Sawatzky, and P. Stamp (Springer, Dordrecht, 2008), p. 151.
[27] S. K. Watson, R. M. Potok, C. M. Marcus, and V. Umansky, Phys. Rev. Lett. **91**, 258301 (2003).
[28] J. Li, A. M. Gilbertson, K. L. Litvinenko, L. F. Cohen, and S. K. Clowes, Phys. Rev. B **85**, 045431 (2012).
[29] C. Yan, S. Kumar, K. Thomas, P. See, I. Farrer, D. Ritchie, J. Griffiths, G. Jones, and M. Pepper, J. Phys.: Condens. Matter **30**, 08LT01 (2018).
[30] D. A. Wharam, T. J. Thornton, R. Newbury, M. Pepper, H. Ahmed, J. E. F. Frost, D. G. Hasko, D. C. Peacock, D. A. Ritchie, and G. A. C. Jones, J. Phys. C **21**, L209 (1988).
[31] B. J. van Wees, H. van Houten, C. W. J. Beenakker, J. G. Williamson, L. P. Kouwenhoven, D. van der Marel, and C. T. Foxon, Phys. Rev. Lett. **60**, 848 (1988).
[32] B. J. van Wees, L. P. Kouwenhoven, E. M. M. Willems, C. J. P. M. Harmans, J. E. Mooij, H. van Houten, C. W. J. Beenakker, J. G. Williamson, and C. T. Foxon, Phys. Rev. B **43**, 12431 (1991).
[33] F. Qu, J. van Veen, F. K. de Vries, A. J. A. Beukman, M. Wimmer, W. Yi, A. A. Kiselev, B.-M. Nguyen, M. Sokolich, M. J. Manfra, F. Nichele, C. M. Marcus, and L. P. Kouwenhoven, Nano Lett. **16**, 7509 (2016).
[34] B. J. LeRoy, A. C. Bleszynski, K. E. Aidala, R. M. Westervelt, A. Kalben, E. J. Heller, S. E. J. Shaw, K. D. Maranowski, and A. C. Gossard, Phys. Rev. Lett. **94**, 126801 (2005).
[35] M. P. Jura, M. A. Topinka, M. Grobis, L. N. Pfeiffer, K. W. West, and D. Goldhaber-Gordon, Phys. Rev. B **80**, 041303 (2009).
[36] N. Paradiso, S. Heun, S. Roddaro, L. Pfeiffer, K. West, L. Sorba, G. Biasiol, and F. Beltram, Physica E **42**, 1038 (2010).
[37] B. Brun, F. Martins, S. Faniel, B. Hackens, G. Bachelier, A. Cavanna, C. Ulysse, A. Ouerghi, U. Gennser, D. Mailly, S. Huant, V. Bayot, M. Sanquer, and H. Sellier, Nat. Commun. **5**, 4290 (2014).
[38] R. Crook, C. G. Smith, A. C. Graham, I. Farrer, H. E. Beere, and D. A. Ritchie, Phys. Rev. Lett. **91**, 246803 (2003).
[39] A. M. Burke, R. Akis, T. E. Day, G. Speyer, D. K. Ferry, and B. R. Bennett, Phys. Rev. Lett. **104**, 176801 (2010).
[40] R. Crook, C. G. Smith, M. Y. Simmons, and D. A. Ritchie, Phys. Rev. B **62**, 5174 (2000).
[41] S. Morikawa, Z. Dou, S.-W. Wang, C. G. Smith, K. Watanabe, T. Taniguchi, S. Masubuchi, T. Machida, and M. R. Connolly, Appl. Phys. Lett. **107**, 243102 (2015).
[42] S. Bhandari, G.-H. Lee, A. Klales, K. Watanabe, T. Taniguchi, E. Heller, P. Kim, and R. M. Westervelt, Nano Lett. **16**, 1690 (2016).
[43] J. H. Davies, I. A. Larkin, and E. V. Sukhorukov, J. Appl. Phys. **77**, 4504 (1995).
[44] A. M. Gilbertson, M. Fearn, J. H. Jefferson, B. N. Murdin, P. D. Buckle, and L. F. Cohen, Phys. Rev. B **77**, 165335 (2008).
[45] K. Kolasiński, B. Szafran, B. Brun, and H. Sellier, Phys. Rev. B **94**, 075301 (2016).
[46] R. M. Potok, J. A. Folk, C. M. Marcus, and V. Umansky, Phys. Rev. Lett. **89**, 266602 (2002).
[47] A. S. Plaut, J. Singleton, R. J. Nicholas, R. T. Harley, S. R. Andrews, and C. T. B. Foxon, Phys. Rev. B **38**, 1323 (1988).
[48] A. Arora, A. Mandal, S. Chakrabarti, and S. Ghosh, J. Appl. Phys. **113**, 213505 (2013).